Journal of Power Sources 438 (2019) 227028

Contents lists available at ScienceDirect

Journal of Power Sources

journal homepage: www.elsevier.com/locate/jpowsour

Al^{3+} ion intercalation pseudocapacitance study of $W_{18}O_{49}$ nanostructure

Mohammad R. Thalji [a], Gomaa A.M. Ali [a,b], H. Algarni [c,d], Kwok Feng Chong [a,*]

[a] Faculty of Industrial Sciences & Technology, Universiti Malaysia Pahang, Gambang, 26300, Kuantan, Malaysia
[b] Chemistry Department, Faculty of Science, Al–Azhar University, Assiut, 71524, Egypt
[c] Research Centre for Advanced Materials Science (RCAMS), King Khalid University, P. O. Box 9004, Abha, 61413, Saudi Arabia
[d] Department of Physics, Faculty of Sciences, King Khalid University, P. O. Box 9004, Abha, Saudi Arabia

HIGHLIGHTS

- A 3D sea urchin-like $W_{18}O_{49}$ nanostructure is prepared by solvothermal route.
- $W_{18}O_{49}$ shows high capacitance in Al^{3+} electrolyte due to ions intercalation.
- Al^{3+} ions intercalate/de-intercalate to cause lattice contraction/expansion.
- Al^{3+} electrolyte as substitute for corrosive acidic electrolyte for $W_{18}O_{49}$.

GRAPHICAL ABSTRACT

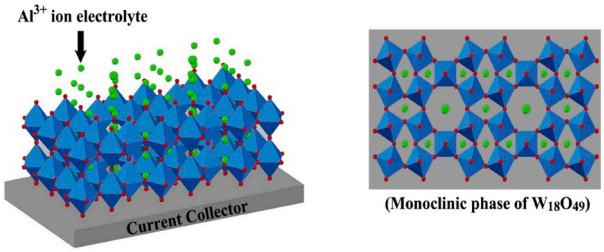

(Intercalation Pseudocapacitance Mechanism)

ARTICLE INFO

Keywords:
Intercalation pseudocapacitance
$W_{18}O_{49}$
Supercapacitors
Charge storage
Al^{3+} electrolyte

ABSTRACT

Intercalation pseudocapacitance is of essential significance for designing high performance electrode materials, which offers exceptional charge storage characteristics. In this study, we elucidate the pseudocapacitive behavior of Al^{3+} ions intercalation within the distinctive tunnels of monoclinic $W_{18}O_{49}$ nanostructure. 3D sea urchin-like $W_{18}O_{49}$ is synthesized through one-step solvothermal approach. Its physicochemical properties are investigated by X-ray diffraction, X-ray photoelectron spectroscopy, Field emission scanning electron microscopy and Brunauer-Emmett-Teller surface area analysis. Cyclic voltammetry, galvanostatic charge-discharge and electrochemical impedance spectroscopy techniques are used to investigate the electrochemical characteristics of $W_{18}O_{49}$ electrode in different electrolyte systems. It shows high specific capacitance of 350 $F\,g^{-1}$ at 1 $A\,g^{-1}$, superior electrochemical long-term stability in the Al^{3+} electrolyte with 92% capacitance retention at 8000 cycles. The excellent electrochemical performance is predominantly due to the Al^{3+} ions intercalation/de-intercalation with $W_{18}O_{49}$ nanostructure that is proven by *ex situ* X-ray diffraction analysis. The work marks a notable achievement in the effort of substituting commonly acidic proton electrolyte for $W_{18}O_{49}$ supercapacitor.

1. Introduction

The global industrialization activities require enormous energy supply that can be sustainably fulfilled by renewable energy sources such as solar, wind and hydro energy. However, the intermittent supply of these energy sources can be the major challenge. In this context, energy storage system can be the solution for the uninterrupted energy supply chain. Among different types of energy storage systems,

* Corresponding author.
E-mail address: ckfeng@ump.edu.my (K.F. Chong).

https://doi.org/10.1016/j.jpowsour.2019.227028
Received 19 May 2019; Received in revised form 22 July 2019; Accepted 16 August 2019
Available online 20 August 2019

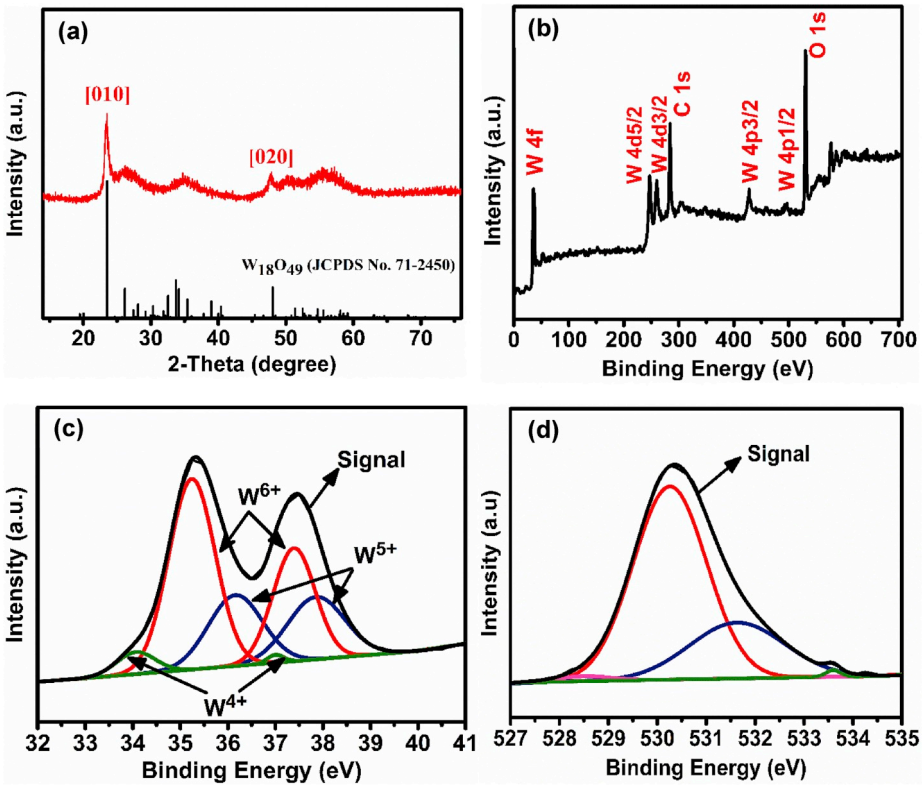

Fig. 1. (a) XRD pattern, (b) XPS wide scan spectrum, (c) XPS narrow scan W4f core level and (d) XPS narrow scan O1s core level of the $W_{18}O_{49}$ nanostructure.

supercapacitors draw great interest due to their high power density, rapid charge-discharge process and theoretical infinite cycle life [1,2]. Nevertheless, their moderate energy density has made them under the great challenge which directly restricts their industrial applications for mass energy supply. This is due to the fact that conventional electrode materials for supercapacitors such as carbon materials are often limited by the non-faradaic process for the charge storage [3–5]. Therefore, substantial research efforts have been devoted to overcoming this limitation [6–8]. The pseudocapacitive materials are under the research spotlight as they offer higher charge storage *via* fast and reversible faradaic reactions at the electrode surface [9,10]. However, such high charge storage behavior is often accompanied by low cycling stability due to structure degradation after prolonged redox reactions. Researchers discovered that by utilizing the intercalation/de-intercalation of ions within the crystal structure, the negative impact of prolonged charge/discharge process can be minimized as this process does not involve any chemical phase transformation [11–13]. This intercalation pseudocapacitance is demonstrated by niobium oxides [14,15], vanadium oxides [13], and tungsten oxides [16].

Tungsten oxides are the *n*-type semiconducting materials of transition metal oxides, with band gap in the range of 2.4–2.8 eV. They are characterized by multi-phase structures which are classified as stoichiometric and sub-stoichiometric oxides based on the lattice distortions that occur to it [17,18]. Amongst different phases, hexagonal phase WO_3 is commonly used as the supercapacitor electrode, due to its distinctive hexagonal and triangular tunnels within the structures. Those tunnels create good cation accommodation, which provides a smooth pathway for charge movement and thus offering rise to the charge storage capability. For instance, Yao et al. [19] reported the electrochemical performance of WO_3 nanorods as the electrode material for supercapacitors and achieved a capacitance of 319.26 F g^{-1} at 0.7 A g^{-1}. Qiu et al. also studied pseudocapacitive performance of electrodeposited WO_3 nanoflowers on Ti foil substrate (196 F g^{-1} at 10 mV s^{-1}) [20]. Recent years, tungsten oxide phase in monoclinic $W_{18}O_{49}$ was also discovered as the emerging electrode material for supercapacitors. Apart from hexagonal and trigonal tunnels, $W_{18}O_{49}$ crystal structure offers additional quadrilateral tunnels that are useful for ions intercalation. Furthermore, the higher oxygen vacancies content in $W_{18}O_{49}$ structure may enhance the electrical conductivity by accelerating electrons diffusion [21]. The charge storage of reduced tungsten oxide was first reported by Yoon et al., which showed the specific capacitance of 199 F g^{-1} in H_2SO_4 electrolyte [22]. Following that, numerous studies also reported $W_{18}O_{49}$ to possess high charge storage ability in H^+ based electrolytes [23,24]. In spite of the remarkable charge storage behavior, it is noteworthy that the strong acidic H^+ based electrolytes may corrode the electrode surface after prolonged usage, thus limiting its electrochemical stability [25,26]. Besides, H^+ reduction could occur to form H_2 gas, which imposes safety issue for supercapacitors [25,27].

Hence, there is urgent need to explore other electrolyte systems for the application of $W_{18}O_{49}$ as supercapacitors electrode. Recently, Al^{3+} ion-based electrolytes receive more interests due to their merits such as low-cost, small ionic radius, high capacity with three-electron redox process and safety for practical applications [28–30]. As compared to the previous report focuses on the electrochemical performance of $W_{18}O_{49}$ and carbon nanotubes composites [26], our current work reports on the electrochemical performance of pure $W_{18}O_{49}$ in different electrolyte systems (LiCl, NaCl, $MgCl_2$ and $AlCl_3$), with detailed elucidation of charge storage mechanisms. Understanding of the charge storage mechanism of pure $W_{18}O_{49}$ in Al^{3+} electrolyte could facilitate the replacement of common acidic electrolyte by the Al^{3+} electrolyte.

2. Experimental section

2.1. Synthesis of the $W_{18}O_{49}$ nanostructure

All chemical reagents (Sigma-Aldrich) were of analytical grade and used as received without further purification. The $W_{18}O_{49}$ nanostructure was prepared through one-pot solvothermal route like previously

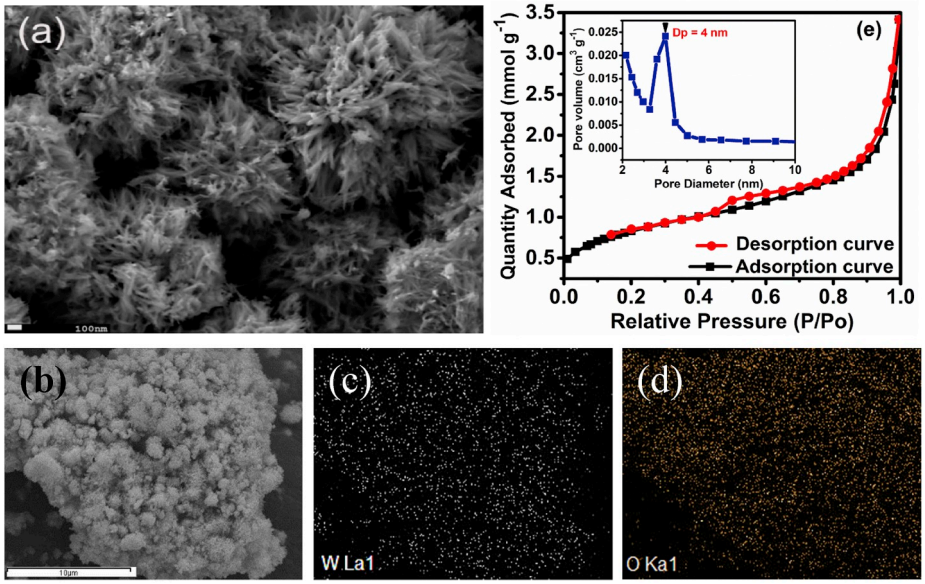

Fig. 2. (a) FESEM image of the 3D sea urchin-like $W_{18}O_{49}$ nanostructure, (b–d) typical FESEM-EDX elemental mapping images for the $W_{18}O_{49}$ nanostructure, (e) N_2 adsorption-desorption isotherm analysis with BJH pore size distribution plot (inset) for the $W_{18}O_{49}$ nanostructure.

reported method [31]. WCl_6 as precursor (W^{6+}, 0.175 g) was first dissolved in an absolute ethanol (30 mL). Next, the solution was sonicated for 10 min at room temperature to form a transparent yellow solution. Subsequently, the solution was carried into a Teflon-lined autoclave which was heated at 200 °C for 10 h. A deep-blue precipitate was finally collected and washed repeatedly with absolute ethanol, followed by vacuum drying at 50 °C overnight.

2.2. Materials characterization

The phase identification of crystalline sample was done by a X-ray diffraction (XRD) diffractometer (Rigaku Miniflex II, Japan), equipped with an automatic divergent slit (Cu-Kα radiation, λ = 0.15418 nm) in the diffraction range from 10° to 80°. The chemical oxidation states of the sample were investigated by X-ray photoelectron spectrometer (XPS, PHI 5000 VersaProbe II, monochromatic Al Kα X-ray source with wide and narrow scan energy of 117.40 eV and 29.35 eV, respectively). The morphology of the sample was observed through a field emission scanning electron microscope (FESEM, JEOL JSM-7800F, USA) operating at 30.0 kV. The N_2 adsorption-desorption isotherms were measured to calculate the Brunauer-Emmett-Teller (BET) surface area and Barrett-Joyner-Halenda (BJH) pore size distribution by a surface area analyzer (Micromeritics ASAP® 2020).

2.3. Electrochemical characterization

The electrochemical measurements were performed at room temperature by a potentiostat-galvanostat (PGSTAT M101, Metrohm Autolab B.V.) in 3-electrode configuration. The working electrode was prepared by thoroughly mixing the active material ($W_{18}O_{49}$ powder, 90 wt%) together with 5 wt% of carbon black and 5 wt% of polyvinylidene difluoride (PVDF) in N-methyl-2-pyrrolidinone (NMP) solvent until it formed a homogenous slurry. The resulting paste was then coated onto a piece of nickel foam electrode as current collector and was dried for 24 h. The electrode was subsequently pressed under 5 MPa to form working electrode with 3–5 mg of active material. A platinum mesh electrode and an Ag/AgCl electrode were used as the counter and reference electrodes, respectively. 1 M LiCl, 1 M NaCl, 1 M $MgCl_2$ and 1 M $AlCl_3$ aqueous solutions were utilized as the electrolytes. Cyclic voltammetry (CV), galvanostatic charge-discharge (GCD) and electrochemical impedance spectroscopy (EIS) tests were conducted to investigate the electrochemical performance of working electrode in different electrolytes. The long-term cycling stability was also performed using GCD measurement at the current density of 5 A g^{-1} for 8000 cycles in $AlCl_3$ electrolyte.

3. Results and discussion

3.1. Structural characterization of $W_{18}O_{49}$ nanostructure

The as-synthesized sample was examined by XRD. As shown in Fig. 1a, the diffraction peaks could be indexed to the monoclinic phase (JCPDS card no. 71-2450, P12/m1) with the lattice constant of a = 17.76 Å, b = 3.80 Å and c = 15.37 Å. The diffraction peaks at 2θ of 23.38° and 47.77° correspond to the (010) and (020), respectively. This indicates the crystal structure growth along b-direction.The sharp peak (010) also indicates the close-packed plane of $W_{18}O_{49}$ crystal and it is in agreement to the previous studies [32–34].

XPS was carried out to identify the elements and their valence states in the as-prepared sample. The fully scanned XPS spectrum confirms the presence of W and O elements without any impurities other than C1s at the binding energy of 284.2 eV which is used as a reference, as seen in Fig. 1b. On the other hand, W4f core level spectrum (Fig. 1c) exhibits three doublet peaks after fitting which are related to the three oxidation states of W atoms.

The first doublet peaks with strong intensity at the binding energies of 35.3 eV and 37.4 eV are attributable to $4f_{7/2}$ and $4f_{5/2}$ for W^{6+}, respectively. The second doublet peaks observed at 36.1 eV and 37.8 eV are resulted from the emission of $W4f_{7/2}$ and $W4f_{5/2}$ core levels from the atoms in an oxidation state of W^{5+}. The third doublet peaks with low intensity at the binding energies of 34.1 eV and 36.9 eV are attributable to W^{4+}. As a sign of the formation of oxygen vacancies, the O1s core level spectrum was further explored through the presence of three peaks (Fig. 1d). A peak is found at the binding energy of 530.3 eV, corresponds to the oxygen bonds with W atom (W–O–W). On the other hand, the second peak at the binding energy of 531.6 eV is attributed to the oxygen atoms in the region of oxygen vacancies which are connected to the reduced W, while the low intensity peak at the binding energy of 533.6 eV corresponds to W–OH. Similar oxidation states of W4f and O1s have been reported in other studies, which confirms the formation of $W_{18}O_{49}$ in this work [35,36]. By examining the FESEM image of the as-synthesized $W_{18}O_{49}$ (Fig. 2a), we observe that it presents as the

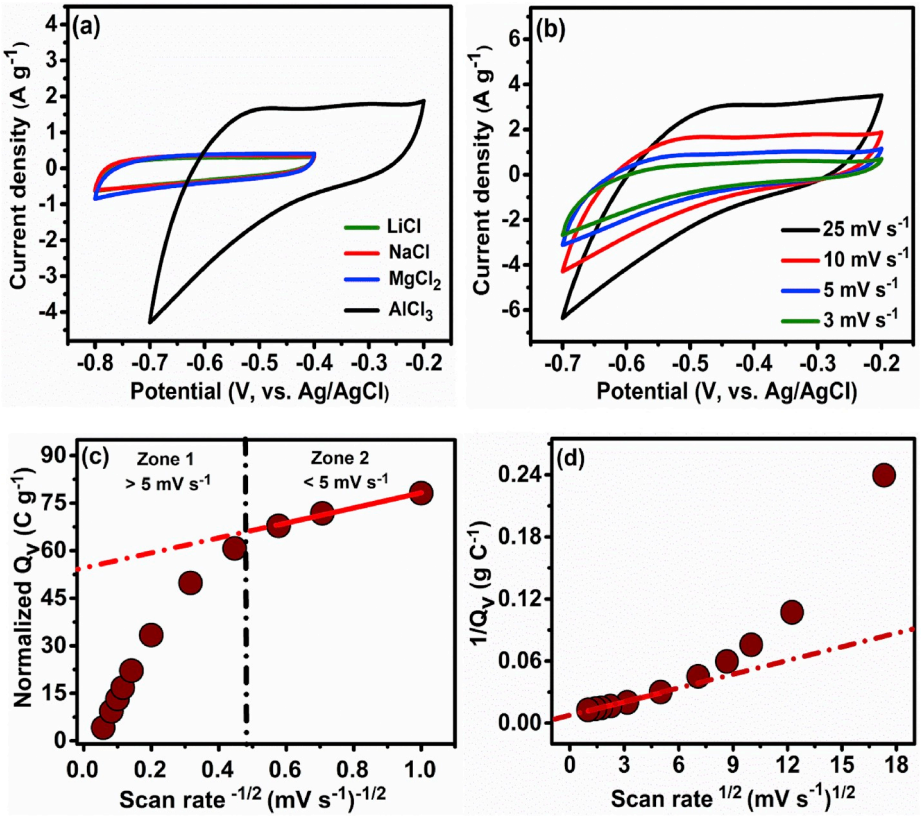

Fig. 3. CV curves of $W_{18}O_{49}$ electrodes in (a) various electrolytes at the scan rate of 10 mV s^{-1} and (b) in $AlCl_3$ electrolyte at different scan rates, (c) normalized Q_V versus $\upsilon^{-1/2}$ and (d) the plot of the reciprocal normalized Q_V versus $\upsilon^{1/2}$ for the $W_{18}O_{49}$ electrodes in $AlCl_3$ electrolyte.

accumulated nanowires (with the average diameter of ca. 30 nm), forming sea urchin-like 3D structure. Furthermore, energy dispersive x-ray analysis (EDX) confirms the presence of W and O only in the as-prepared sample, as shown in Fig. 2b–d. The elemental maps also display the well-distribution of both W and O elements with the atomic proportions of 26.83% and 73.17% for W and O elements, respectively (Fig. S1).

Good surface area properties are expected from the distinctive morphology of $W_{18}O_{49}$. As shown in Fig. 2e, the N_2 adsorption-desorption isotherm curve of the $W_{18}O_{49}$ shows the Type (IV) isotherm with BET surface area and pore radius of 68.23 m^2 g^{-1} and 4 nm, respectively. The mesoporous $W_{18}O_{49}$ could provide sufficient ions diffusion channels to enhance the electrochemical performance.

3.2. Electrochemical characterization

The electrochemical performance and charge storage mechanism of $W_{18}O_{49}$ were investigated using CV, GCD and EIS techniques in different aqueous electrolytes (LiCl, NaCl, $MgCl_2$ and $AlCl_3$). The optimal electrochemical window was determined by choosing open circuit potential as the upper potential limit; and the lower potential limit was determined by stepwise decreasing the lower potential before any electrolyte decomposition was observed [37]. Fig. 3a reveals the optimal CV windows of $W_{18}O_{49}$ in different electrolytes at scan rate of 10 mV s^{-1}. Bubbling due to electrolyte redox reaction was observed if the potential was applied beyond the optimal CV windows. All CV curves show rectangular shape, which indicates the highly capacitive behavior of $W_{18}O_{49}$ (Fig. S2). It is worth noting that for $AlCl_3$ electrolyte, the $W_{18}O_{49}$ shows the CV curve with larger capacitive window and an oxidation peak at ca. −0.5 V, which is more obvious at lower scan rates Fig. 3b. This possible pseudocapacitive behavior motivates us to further investigate the charge storage mechanism of $W_{18}O_{49}$ in $AlCl_3$ electrolyte, *via* Trasatti's analysis.

The total amount of stored charges (Q_T) in the electrode material are united between two components, as shown in Eq. (1) [38,39]:

$$Q_T = Q_C + Q_D \quad (1)$$

Where Q_C is the capacitive charge storage from both double layer and pseudocapacitive behaviors and Q_D is the diffusive charge storage. On the basis of Eq. (1), the dominant charge storage process can be estimated by the following Equations:

$$Q_V = Q_C + \alpha\upsilon^{-1/2} \quad (2)$$

$$\frac{1}{Q_V} = \frac{1}{Q_T} + \alpha\upsilon^{1/2} \quad (3)$$

Where Q_V is the total measured voltammetric charge, α is a constant and υ represents the scan rate.

Based on Eq. (2), the Q_C can be obtained as intercept by extrapolating the plot of Q_V vs. $\upsilon^{-1/2}$, with deeming infinite-diffusion during charging/discharging processes. Fig. 3c shows the plot of Q_V vs. $\upsilon^{-1/2}$ for $W_{18}O_{49}$ electrode in $AlCl_3$ electrolyte at scan rates between 1 and 300 mV s^{-1}. The linear zone (zone 1: >5 mV s^{-1}), which the Q_V is sensitive to the change of scan rates, represents the diffusion behavior. On the other hand, the second zone (zone 2: <5 mV s^{-1}) represents the capacitive contribution, which is independent of the scan rates. As a result, the extrapolation of Q_V in zone (2) produces Q_C to indicate the capacitive process. The Q_C values of $W_{18}O_{49}$ in $AlCl_3$ electrolyte is measured to be 54.31 C g^{-1} and it is higher than that of the other three electrolytes, which are 21.11 C g^{-1}, 24.40 C g^{-1} and 24.93 C g^{-1} for LiCl, NaCl and $MgCl_2$ electrolytes, respectively (Fig. S3a). This could be associated to the higher charge density of Al^{3+} ions.

In order to confirm the dominant charge storage mechanism, Q_T is obtained as intercept (υ approaching 0) through extrapolation of the

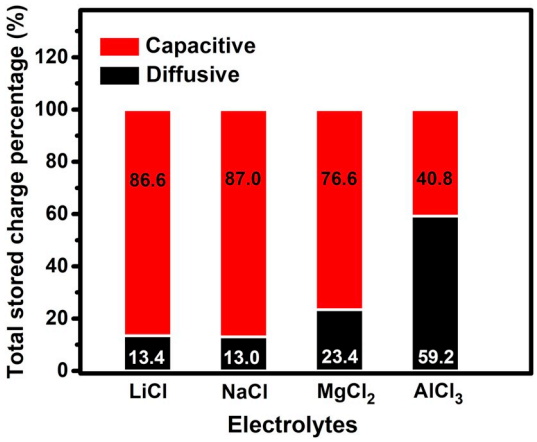

Fig. 4. The ratio of the charge storage contribution (capacitive and diffusive) for the $W_{18}O_{49}$ electrodes in different electrolytes.

plot $1/Q_V$ vs. $\upsilon^{1/2}$ as Fig. 3d. The Q_T for $W_{18}O_{49}$ in $AlCl_3$ electrolyte is 132.98 C g^{-1}, which is higher as compared to that of LiCl, NaCl and $MgCl_2$ of 24.40, 27.70 and 32.53 C g^{-1}, respectively (Fig. S3b). As Eq. (1), the Q_D values can be obtained and their contribution in Q_T is summarized as Fig. 4. It can be clearly seen that the charge storage of $W_{18}O_{49}$ in LiCl, NaCl and $MgCl_2$ are mostly contributed by capacitive charge storage (>76% of total charge storage), which involves the adsorption of ions on electrode surface. On the contrary, diffusive charge storage contributes 59.2% of the total charge storage of $W_{18}O_{49}$ in $AlCl_3$ electrolyte. This indicates that apart from ions adsorption, the ions diffusion within the electrode material also contributes to its charge storage, which can be associated to the ions intercalation within the electrode [40,41].

Fig. 5 shows the optimal GCD curves of $W_{18}O_{49}$ electrode in different electrolytes. Similar potential range as CV was adapted to avoid redox reaction of the electrolytes. The GCD curves of $W_{18}O_{49}$ electrode are unequivocally reversible in different electrolytes. However, significant *iR* drop can be observed in the range of (−0.40 to −0.45 V) for GCD curves in LiCl, NaCl and $MgCl_2$ electrolytes. This could be associated to the low molar ionic conductivity and ionic mobility of LiCl, NaCl and $MgCl_2$ electrolytes, as tabulated in Table S1. The high *iR* drop is unfavorable for the industrial application as it could lead to huge power loss. $W_{18}O_{49}$ electrode in $AlCl_3$ electrolyte exhibits GCD curves with insignificant *iR* drop and longest discharge time, as compared to that in other electrolytes. Meanwhile, a small potential plateau is observed for GCD curve of $W_{18}O_{49}$ electrode in $AlCl_3$ electrolyte at 1 A g^{-1}, which can be attributed to the Al^{3+} ions intercalation into $W_{18}O_{49}$ crystal lattice [42,43]. This potential plateau is insignificant at higher current densities, possibly due to the fast charging that limits the intercalation process.

The specific capacitance was calculated from GCD curves [44] and summarized in Fig. 6a. The highest specific capacitance of 350 F g^{-1} is attained in $AlCl_3$ at 1 A g^{-1}, followed by low specific capacitance values in LiCl (36.0 F g^{-1}), NaCl (42.5 F g^{-1}) and $MgCl_2$ (40.0 F g^{-1}). This can be explained by the intrinsic properties of $AlCl_3$ electrolyte. As compared to other electrolytes, $AlCl_3$ has the highest molar ionic conductivity of 9.38 mS m^2 mol^{-1} and ionic mobility of 6.50×10^{-8} m^2 s^{-1} V^{-1}, which promotes charge transfer and convection mass transfer, respectively. Furthermore, in strong acid (pH < 3), the octahedral structure of hydrated $Al(H_2O)_6^{3+}$ ion is dominant through the hydrolysis process and Al^{3+} ions exist almost entirely in the solution [45]. In current work, the pH value of 1 M $AlCl_3$ electrolyte is 2.13, which reflects total H^+ concentration of 7.413×10^{-3} M. Hence, CV and GCD tests had been conducted in 7.413×10^{-3} M HCl electrolyte (pH ~ 2.13), as shown in Fig. S4. It is clear that the H^+ intercalation contributes insignificantly in the current Al^{3+} system where [H^+] is merely 7.413×10^{-3} M.

It should be noted that Al^{3+} possesses the lowest hydrated ionic radius of 1.89 Å, which accommodates higher ions adsorption on electrode surface for charge storage [46,47]. Its lowest hydrated ionic radius also motivates further investigation of possible insertion of Al^{3+} into $W_{18}O_{49}$ crystal structure during charge/discharge process. Fig. 6b shows the *ex situ* XRD investigation of $W_{18}O_{49}$ electrode during fully charged/discharged processes in $AlCl_3$ electrolyte. It is worth mentioning that the [010] peak of $W_{18}O_{49}$ shifts to higher diffraction angle after

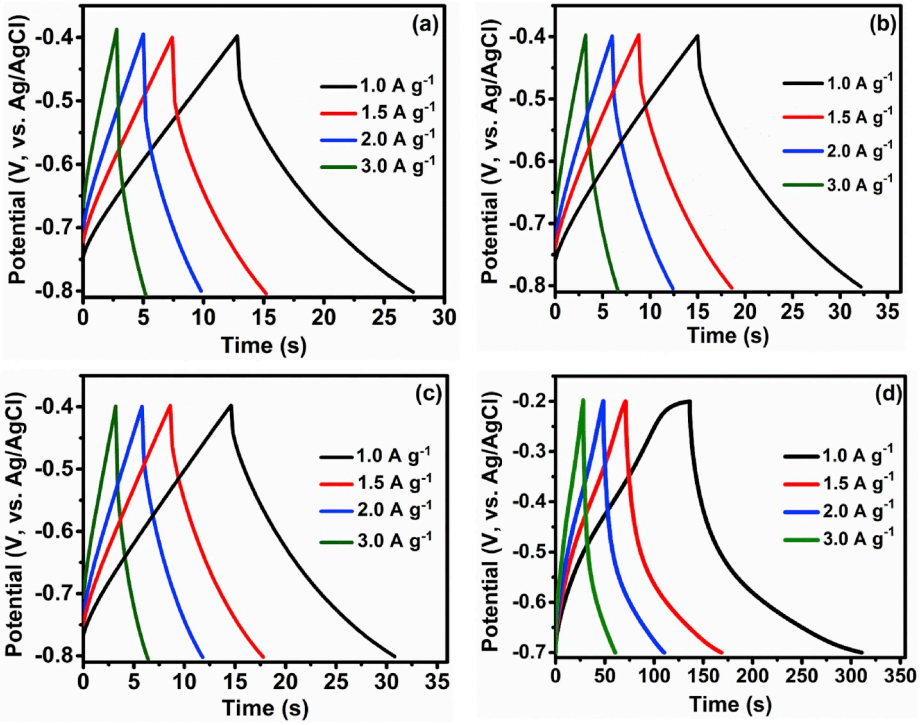

Fig. 5. Galvanostatic charge/discharge profiles for $W_{18}O_{49}$ electrodes in (a) LiCl, (b) NaCl, (c) $MgCl_2$ and (d) $AlCl_3$ electrolytes at different current densities.

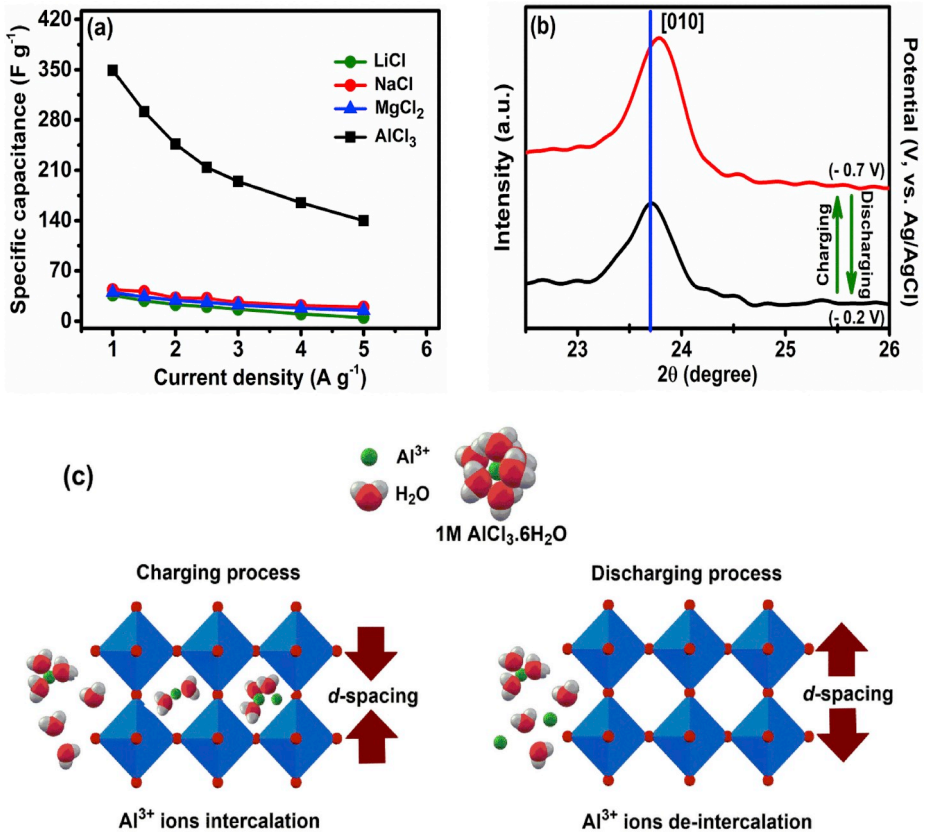

Fig. 6. (a) Specific capacitance of $W_{18}O_{49}$ electrodes in different electrolytes as a function of current density, (b) *Ex situ* XRD investigation of $W_{18}O_{49}$ electrode after fully charged and discharged in $AlCl_3$ electrolyte, (c) schematic illustration of interlayer expansion/contraction of $W_{18}O_{49}$ after Al^{3+} de-intercalation/intercalation during GCD process.

fully charged process, indicating interlayer spacing decrease ($d = 3.73$ Å). When Al^{3+} ions intercalate into the interlayers of $W_{18}O_{49}$ crystal structure, there is electrostatic interaction between the positive Al^{3+} ions and polar atoms in the crystal structure, leading to the lattice contraction and the interlayer spacing decrease [48]. On the other hand, the [010] peak shifts to lower diffraction angle with higher interlayer spacing ($d = 3.75$ Å), upon fully discharged process. The interlayer expansion is attributed to the de-intercalation of Al^{3+} ions from the $W_{18}O_{49}$ crystal structure. Such phenomenon is illustrated as Fig. 6c and it is also corroborated by the Trasatti's analysis to suggest diffusive charge storage as the dominant energy storage mechanism. All these analyses suggest that the high capacitance of $W_{18}O_{49}$ in $AlCl_3$ electrolyte is due to the intercalation of Al^{3+} ions into various tunnels in the monoclinic $W_{18}O_{49}$ crystal lattice. On the other hand, the low capacitance values of $Li^+/Na^+/Mg^{2+}$ systems could be due to their larger hydrated ionic radii, as compared to that of Al^{3+} system. The larger ionic radii causes the hydrated ions to diffuse slower and they are too big (hydrated ionic radii for Li^+ (2.10 Å); Na^+ (2.43 Å) and Mg^{2+} (2.10 Å)) to intercalate within $W_{18}O_{49}$ crystal structure (*d*-spacing of = 3.80 Å). The absence of intercalation pseudocapacitance in $Li^+/Na^+/Mg^{2+}$ system causes them to exhibit lower charge storage behavior.

EIS testing was carried out to acquire charge kinetics of $W_{18}O_{49}$ electrode in different electrolytes. As shown in Fig. 7a, the quasi-semicircle at the high-frequency region in Nyquist plots corresponds to the interfacial charge transfer resistance (R_{CT}), while the first intersection point at the real impedance (Z′) represents the equivalent series resistance (ESR) which is the combination of ionic resistance of the

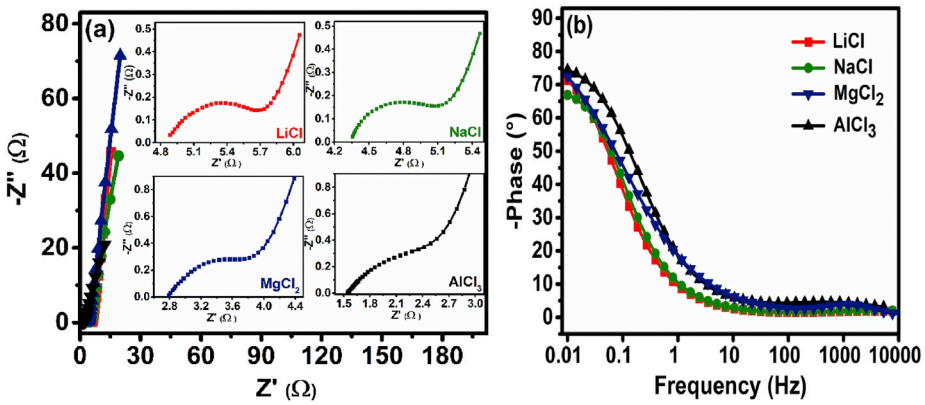

Fig. 7. (a) The Nyquist plots (the insets show the high frequency region) and (b) Bode plots for $W_{18}O_{49}$ electrodes in different electrolytes.

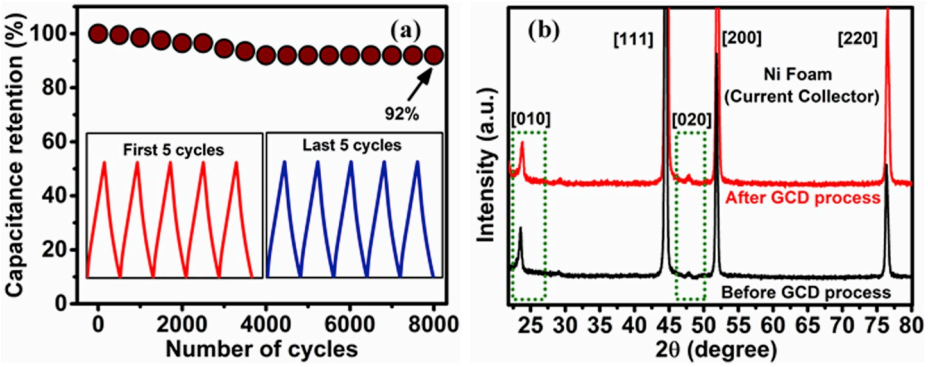

Fig. 8. (a) Cycling stability of $W_{18}O_{49}$ electrode in $AlCl_3$ electrolyte at the current density of 5 A g^{-1} (Insets show the GCD curves for the first 5 cycles and last 5 cycles) and (b) XRD patterns of the pristine $W_{18}O_{49}$ electrode material before and after GCD process.

electrolyte and intrinsic resistance of the electroactive material. From the insets of Fig. 7a, it can be clearly seen that the ESR value of $W_{18}O_{49}$ electrode in $AlCl_3$ electrolyte is the lowest as compared to those in LiCl, NaCl and $MgCl_2$ electrolytes, which can be associated to the higher ionic conductivity of $AlCl_3$ electrolyte. Furthermore, the $W_{18}O_{49}$ electrode also experiences lower Warburg impedance in $AlCl_3$ electrolyte, by having shorter impedance line at low frequency region. This signifies the lower diffusion resistance of Al^{3+} ions in $W_{18}O_{49}$ crystal structure.

The EIS data are further analyzed to obtain the electrochemically active surface area of the electrode material (S_E), using Eq. (4) [49,50]:

$$S_E = C_{dm}/C_d \quad (4)$$

Where, $C_{dm} = (2\pi fmZ'')^{-1}$, Z'' is the imaginary impedance from Nyquist plots at the frequency (10 mHz) and C_d is a constant value of 60 μF cm^{-2} for metal oxide electrode. The S_E value for $W_{18}O_{49}$ is the highest in $AlCl_3$ electrolyte with 166.2 m^2 g^{-1}, which is higher than those in LiCl (81.80 m^2 g^{-1}), NaCl (79.30 m^2 g^{-1}) and $MgCl_2$ (67.50 m^2 g^{-1}). The smallest hydrated Al^{3+} ions could adsorb more onto electrode surface, in addition to its ability to diffuse and intercalate within $W_{18}O_{49}$ structure, contributing to higher electrochemically active surface area. The relationship of the phase angle on the frequency using different electrolytes is illustrated in Fig. 7b. For the $AlCl_3$ electrolyte, the phase angle of $W_{18}O_{49}$ electrode reaches 74.4°, which is higher than 72.4°, 71.3° and 66.9° for the $MgCl_2$, LiCl and NaCl electrolytes, respectively. This indicates a good capacitive performance as the ideal capacitor phase angle is 90° [51]. Moreover, additional evaluation on the frequency response can be obtained by comparing the characteristic frequency (f^* at a phase angle of 45°) which is corresponding to the minimum time needs to discharge all the energy from the device with an efficiency of greater than 50%. The relaxation time (τ) was calculated using Eq. (5) [52]:

$$\tau = 1/2\pi f^* \quad (5)$$

$W_{18}O_{49}$ electrode exhibits the lowest τ value of 0.59 s in $AlCl_3$ electrolyte, which is much lower than that in LiCl (2.55 s), NaCl (1.76 s) and $MgCl_2$ (1.47 s). It also demonstrates the potential of $AlCl_3$ to be used as the electrolyte for high performance $W_{18}O_{49}$ supercapacitor electrode.

$W_{18}O_{49}$ supercapacitor electrode cycling stability in $AlCl_3$ electrolyte is tested for 8000 GCD cycles at 5 A g^{-1}. As shown in Fig. 8a, the $W_{18}O_{49}$ electrode maintains at 92% capacitance retention at the end of 8000 GCD cycles. In addition, the GCD curves shape also maintain, as shown in Fig. 8a insets. The high stability of $W_{18}O_{49}$ electrode in $AlCl_3$ electrolyte renders it to be the supercapacitor for long term usage. Furthermore, the structural stability of $W_{18}O_{49}$ electrode before and after GCD process were investigated by XRD and found that it maintains its original crystal structure without significant collapse, as shown in Fig. 8b.

4. Conclusions

A comprehensive study has been conducted to investigate different electrolytes (LiCl, NaCl, $MgCl_2$ and $AlCl_3$) performance as the electrolyte for $W_{18}O_{49}$ supercapacitor electrode. The distinctive crystal structure of $W_{18}O_{49}$ (d-spacing = 3.8 Å) allows the intercalation of small size Al^{3+} ions, contributing to the highest electrochemical performance. The findings suggest the alternative electrolyte to replace highly corrosive acidic electrolyte for the $W_{18}O_{49}$ supercapacitor electrode.

Declarations of interest

None.

Acknowledgments

The authors would like to acknowledge the funding from the Ministry of Education Malaysia in the form of [RDU170113: FRGS/1/2017/STG07/UMP/01/1] and Universiti Malaysia Pahang grant RDU170357. Moreover, the authors extend their appreciation to King Khalid University, the Ministry of Education – Kingdom of Saudi Arabia for supporting this research through a grant (RCAMS/KKU/002-18) under research center for advanced material science.

Appendix A. Supplementary data

Supplementary data to this article can be found online at https://doi.org/10.1016/j.jpowsour.2019.227028.

References

[1] I.K. Chakraborty, N. Chakrabarty, A. Senapati, A.K. Chakraborty, CuO@NiO/Polyaniline/MWCNT nanocomposite as high performance electrode for supercapacitor, J. Phys. Chem. C 122 (2018) 27180–27190. https://doi:10.1021/acs.jpcc.8b08091.

[2] G. Yu, L. Hu, N. Liu, H. Wang, M. Vosgueritchian, Y. Yang, Y. Cui, Z. Bao, Enhancing the supercapacitor performance of graphene/MnO_2 nanostructured electrodes by conductive wrapping, Nano Lett. 11 (2011) 4438–4442. https://doi:10.1021/nl2026635.

[3] Z.H. Huang, Y. Song, D.Y. Feng, Z. Sun, X. Sun, X.X. Liu, High mass loading MnO_2 with hierarchical nanostructures for supercapacitors, ACS Nano 12 (2018) 3557–3567. https://doi:10.1021/acsnano.8b00621.

[4] A. Sarkar, A.K. Chakraborty, S. Bera, S. Krishnamurthy, Novel hydrothermal synthesis of CoS_2/MWCNT nanohybrid electrode for supercapacitor: a systematic investigation on the influence of MWCNT, J. Phys. Chem. C 122 (2018) 18237–18246. https://doi:10.1021/acs.jpcc.8b04137.

[5] W. Guo, C. Yu, S. Li, Z. Wang, J. Yu, H. Huang, J. Qiu, Strategies and insights towards the intrinsic capacitive properties of MnO_2 for supercapacitors: challenges and perspectives, Nano Energy 57 (2018) 459–472. https://doi:10.1016/j.nanoen.2018.12.015.

[6] X. Qi, W. Zheng, X. Li, G. He, Multishelled NiO hollow microspheres for high-performance supercapacitors with ultrahigh energy density and robust cycle life, Sci. Rep. 6 (2016) 1–10. https://doi:10.1038/srep33241.

[7] S. Liu, S.C. Lee, U.M. Patil, C. Ray, K.V. Sankar, K. Zhang, A. Kundu, S. kang, J. H. Park, S.C. Jun, Controllable sulfuration engineered NiO nanosheets with enhanced capacitance for high rate supercapacitors, J. Mater. Chem. A 5 (9) (2017) 4543–4549. https://doi:10.1039/C6TA11049E.

[8] D.P. Dubal, O. Ayyad, V. Ruiz, P. Gómez-Romero, Hybrid energy storage: the merging of battery and supercapacitor chemistries, Chem. Soc. Rev. 44 (2015) 1777–1790. https://doi:10.1039/c4cs00266k.

[9] G. Zhu, C. Xi, M. Shen, C. Bao, J. Zhu, Nanosheet-based hierarchical $Ni_2(CO_3)(OH)_2$ microspheres with weak crystallinity for high-performance supercapacitor, ACS Appl. Mater. Interfaces 6 (2014) 17208–17214. https://doi:10.1021/am505056d.

[10] S. Devaraj, N. Munichandraiah, Effect of crystallographic structure of MnO_2 on its electrochemical capacitance properties, J. Phys. Chem. C 112 (2008) 4406–4417. https://doi:10.1021/jp7108785.

[11] M. Salanne, B. Rotenberg, K. Naoi, K. Kaneko, P.L. Taberna, C.P. Grey, B. Dunn, P. Simon, Efficient storage mechanisms for building better supercapacitors, Nat. Energy 1 (2016) 16070–16080. https://doi:10.1038/nenergy.2016.70.

[12] Y. Wang, Y. Song, Y. Xia, Electrochemical capacitors: mechanism, materials, systems, characterization and applications, Chem. Soc. Rev. 45 (2016) 5925–5950. https://doi:10.1039/c5cs00580a.

[13] T. Jin, H. Li, Y. Li, L. Jiao, J. Chen, Intercalation pseudocapacitance in flexible and self-standing V_2O_3 porous nanofibers for high-rate and ultra-stable K ion storage, Nano Energy 50 (2018) 462–467. https://doi:10.1016/j.nanoen.2018.05.056.

[14] V. Augustyn, J. Come, M.A. Lowe, J.W. Kim, P.L. Taberna, S.H. Tolbert, H. D. Abruña, P. Simon, B. Dunn, High-rate electrochemical energy storage through Li^+ intercalation pseudocapacitance, Nat. Mater. 12 (2013) 518–522. https://doi:10.1038/nmat3601.

[15] S. Lou, X. Cheng, L. Wang, J. Gao, Q. Li, Y. Ma, Y. Gao, P. Zuo, C. Du, G. Yin, High-rate capability of three-dimensionally ordered macroporous T-Nb_2O_5 through Li^+ intercalation pseudocapacitance, J. Power Sources 361 (2017) 80–86. https://doi:10.1016/j.jpowsour.2017.06.023.

[16] M. Zhu, W. Meng, Y. Huang, Y. Huang, C. Zhi, Proton-insertion-enhanced pseudocapacitance based on the assembly structure of tungsten oxide, ACS Appl. Mater. Interfaces 6 (2014) 18901–18910. https://doi:10.1021/am504756u.

[17] S. Cong, F. Geng, Z. Zhao, Tungsten oxide materials for optoelectronic applications, Adv. Mater. 28 (2016) 10518–10528. https://doi:10.1002/adma.201601109.

[18] H. Zheng, J.Z. Ou, M.S. Strano, R.B. Kaner, A. Mitchell, K. Kalantar-Zadeh, Nanostructured tungsten oxide - properties, synthesis, and applications, Adv. Funct. Mater. 21 (2011) 2175–2196. https://doi:10.1002/adfm.201002477.

[19] S. Yao, F. Qu, G. Wang, X. Wu, Facile hydrothermal synthesis of WO_3 nanorods for photocatalysts and supercapacitors, J. Alloy. Comp. 724 (2017) 695–702. https://doi:10.1016/j.jallcom.2017.07.123.

[20] M. Qiu, P. Sun, L. Shen, K. Wang, S. Song, X. Yu, S. Tan, C. Zhao, W. Mai, WO_3 nanoflowers with excellent pseudo-capacitive performance and the capacitance contribution analysis, J. Mater. Chem. A 4 (2016) 7266–7273. https://doi:10.1039/c6ta00237d.

[21] K. Bao, W. Mao, G. Liu, L. Ye, H. Xie, S. Ji, D. Wang, C. Chen, Y. Li, Preparation and electrochemical characterization of ultrathin WO_{3-x}/C nanosheets as anode materials in lithium ion batteries, Nano Res. 10 (2017) 1903–1911. https://doi:10.1007/s12274-016-1373-6.

[22] S. Yoon, E. Kang, J.K. Kim, C.W. Lee, J. Lee, Development of high-performance supercapacitor electrodes using novel ordered mesoporous tungsten oxide materials with high electrical conductivity, Chem. Commun. 47 (2011) 1021–1023. https://doi:10.1039/C0CC03594G.

[23] S. Park, H.W. Shim, C.W. Lee, H.J. Song, J.C. Kim, D.W. Kim, High-power and long-life supercapacitive performance of hierarchical, 3-D urchin-like $W_{18}O_{49}$ nanostructure electrodes, Nano Res. 9 (2016) 633–643. https://doi:10.1007/s12274-015-0943-3.

[24] J. Jung, D.H. Kim, $W_{18}O_{49}$ nanowires assembled on carbon felt for application to supercapacitors, Appl. Surf. Sci. 433 (2018) 750–755. https://doi:10.1016/j.apsusc.2017.10.109.

[25] Y. Tian, W. Zhang, S. Cong, Y. Zheng, F. Geng, Z. Zhao, Unconventional aluminum ion intercalation/deintercalation for fast switching and highly stable electrochromism, Adv. Funct. Mater. 25 (2015) 5833–5839. https://doi:10.1002/adfm.201502638.

[26] K. Li, Y. Shao, S. Liu, Q. Zhang, H. Wang, Y. Li, R.B. Kaner, Aluminum-ion-intercalation supercapacitors with ultrahigh areal capacitance and highly enhanced cycling stability: power supply for flexible electrochromic devices, Small 13 (2017) 1–10. https://doi:10.1002/smll.201700380.

[27] S.J. Yoo, J.W. Lim, Y.E. Sung, Y.H. Jung, H.G. Choi, D.K. Kim, Fast switchable electrochromic properties of tungsten oxide nanowire bundles, Appl. Phys. Lett. 90 (2007) 88–91. https://doi:10.1063/1.2734395.

[28] Y. Hu, D. Sun, B. Luo, L. Wang, Recent progress and future trends of aluminum batteries, Energy Technol. 7 (2019) 86–106. https://doi:10.1002/ente.201800550.

[29] Y. Hu, B. Luo, D. Ye, X. Zhu, M. Lyu, L. Wang, An innovative freeze-dried reduced graphene oxide supported SnS_2 cathode active material for aluminum-ion batteries, Adv. Mater. 29 (48) (2017) 1606132–1606137. https://doi:10.1002/adma.201606132.

[30] L. Li, B. Luo, S. Peng, S. Wang, Y. Hu, H. Hu, D. Ye, L. Wang, X. Zhu, A binder-free and free-standing cobalt sulfide@carbon nanotube cathode material for aluminum-ion batteries, Adv. Mater. 30 (2017) 1703824–1703829. https://doi:10.1002/adma.201703824.

[31] G. Xi, S. Ouyang, P. Li, J. Ye, Q. Ma, N. Su, H. Bai, C. Wang, Ultrathin $W_{18}O_{49}$ nanowires with diameters below 1 nm: synthesis, near-infrared absorption, photoluminescence, and photochemical reduction of carbon dioxide, Angew. Chem. Int. Ed. 51 (2012) 2395–2399. https://doi:10.1002/anie.201107681.

[32] W. Xu, Q. Tian, Z. Chen, M. Xia, D.K. Macharia, B. Sun, L. Tian, Y. Wang, M. Zhu, Optimization of photothermal performance of hydrophilic $W_{18}O_{49}$ nanowires for the ablation of cancer cells in vivo, J. Mater. Chem. B 2 (2014) 5594–5601. https://doi:10.1039/c4tb00669k.

[33] Y. Sun, W. Wang, J. Qin, D. Zhao, B. Mao, Y. Xiao, M. Cao, Oxygen vacancy-rich mesoporous $W_{18}O_{49}$ nanobelts with ultrahigh initial coulombic efficiency toward high-performance lithium storage, Electrochim. Acta 187 (2016) 329–339. https://doi:10.1016/j.electacta.2015.11.064.

[34] D. Wang, J. Li, X. Cao, G. Pang, S. Feng, Hexagonal mesocrystals formed by ultra-thin tungsten oxide nanowires and their electrochemical behaviour, Chem. Commun. 46 (2010) 7718–7720. https://doi:10.1039/c0cc01835j.

[35] N. Zhang, Y. Zhao, Y. Lu, G. Zhu, Preparation of aligned $W_{18}O_{49}$ nanowire clusters with high photocatalytic activity, Mater. Sci. Eng. B Solid State Mater. Adv. Technol. 218 (2017) 51–58. https://doi:10.1016/j.mseb.2017.02.004.

[36] G. Hai, J. Huang, L. Cao, Y. Jie, J. Li, X. Wang, Shape evolution of hierarchical $W_{18}O_{49}$ nanostructures: a systematic investigation of the growth mechanism, properties and morphology-dependent photocatalytic activities, Nanomaterials 6 (2016) 240–252. https://doi:10.3390/nano6120240.

[37] M. Lukatskaya, O. Mashtalir, C. Ren, Y. Agnese, P. Rozier, P. Taberna, M. Naguib, P. Simon, M. Barsoum, Y. Gogotsi, Cation intercalation and high volumetric capacitance of two-dimensional titanium carbide, Science 341 (2013) 1502–1505. https://doi:10.1126/science.1241488.

[38] E.A.A. Aboelazm, G.A.M. Ali, H. Algarni, H. Yin, Y.L. Zhong, K.F. Chong, Magnetic electrodeposition of the hierarchical cobalt oxide nanostructure from spent lithium-ion batteries: its application as a supercapacitor electrode, J. Phys. Chem. C 122 (2018) 12200–12206. https://doi:10.1021/acs.jpcc.8b03306.

[39] G.A.M. Ali, M.M. Yusoff, H. Algarni, K.F. Chong, One-step electrosynthesis of MnO_2/rGO nanocomposite and its enhanced electrochemical performance, Ceram. Int. 44 (2018) 7799–7807. https://doi:10.1016/j.ceramint.2018.01.212.

[40] K.M. Hercule, Q. Wei, O.K. Asare, L. Qu, A.M. Khan, M. Yan, C. Du, W. Chen, L. Mai, Interconnected nanorods-nanoflakes $Li_2Co_2(MoO_4)_3$ framework structure with enhanced electrochemical properties for supercapacitors, Adv. Energy Mater. 5 (2015) 1–7. https://doi:10.1002/aenm.201500060.

[41] T. Brezesinski, J. Wang, S.H. Tolbert, B. Dunn, Ordered mesoporous α-MoO_3 with iso-oriented nanocrystalline walls for thin-film pseudocapacitors, Nat. Mater. 9 (2010) 146–151. https://doi:10.1038/nmat2612.

[42] C. Zhang, Y. Xie, J. Wang, A. Pentecost, D. Long, L. Ling, Effect of graphitic structure on electrochemical ion intercalation into positive and negative electrodes, J. Solid State Electrochem. 18 (2014) 2673–2682. https://doi:10.1007/s10008-014-2527-7.

[43] B.H. Ka, S.M. Oh, Electrochemical activation of expanded graphite electrode for electrochemical capacitor, J. Electrochem. Soc. 155 (2008) 685–692. https://doi:10.1149/1.2953525.

[44] S.H. Lee, C. Park, J.W. Park, S.J. Kim, S.S. Im, H. Ahn, Synthesis of conducting polymer-intercalated vanadate nanofiber composites using a sonochemical method for high performance pseudocapacitor applications, J. Power Sources 414 (2019) 460–469. https://doi:10.1016/j.jpowsour.2019.01.031.

[45] T.W. Swaddle, J. Rosenqvist, P. Yu, E. Bylaska, B.L. Phillips, W.H. Casey, Kinetic evidence for five-coordination in $AlOH^{2+}_{(aq)}$ ion, Science 308 (2005) 1450–1453. https://doi:10.1126/science.1110231.

[46] I. Persson, Hydrated metal ions in aqueous solution: how regular are their structures? Pure Appl. Chem. 82 (2010) 1901–1917. https://doi:10.1351/PAC-CON-09-10-22.

[47] Z. Li, K. Xiang, W. Xing, W.C. Carter, Y.M. Chiang, Reversible aluminum-ion intercalation in prussian blue analogs and demonstration of a high-power aluminum-ion asymmetric capacitor, Adv. Energy Mater. 5 (2015) 1–6. https://doi:10.1002/aenm.201401410.

[48] K. Li, Y. Shao, H. Yan, Z. Lu, K.J. Griffith, J. Yan, G. Wang, H. Fan, J. Lu, W. Huang, B. Bao, X. Liu, C. Hou, Q. Zhang, Y. Li, J. Yu, H. Wang, Lattice-contraction triggered synchronous electrochromic actuator, Nat. Commun. 9 (2018) 4798–4808. https://doi:10.1038/s41467-018-07241-7.

[49] I. Electroanal, U. Milano, Real surface area measurements, Electroanal. Chem. 327 (1993) 353–376.

[50] G.A.M. Ali, M.M. Yusoff, E.R. Shaaban, K.F. Chong, High performance MnO_2 nanoflower supercapacitor electrode by electrochemical recycling of spent batteries, Ceram. Int. 43 (2017) 8440–8448. https://doi:10.1016/j.ceramint.2017.03.195.

[51] V. Augustyn, P. Simon, B. Dunn, Pseudocapacitive oxide materials for high-rate electrochemical energy storage, Energy Environ. Sci. 7 (2014) 1597–1614. https://doi:10.1039/c3ee44164d.

[52] G.S. Gund, D.P. Dubal, B.H. Patil, S.S. Shinde, C.D. Lokhande, Enhanced activity of chemically synthesized hybrid graphene oxide/Mn_3O_4 composite for high performance supercapacitors, Electrochim. Acta 92 (2013) 205–215. https://doi:10.1016/j.electacta.2012.12.120.